Heterojunction Structure of Cobalt Sulfide Cathodes for High-Performance Magnesium-Ion Batteries

Jianbiao Wang,[1] Tanmay Ghosh,[1] Zhengyu Ju,[2] Man-Fai Ng,[3] Gang Wu,[3] Gaoliang Yang,[1] Xiaofei Zhang,[1] Lei Zhang,[1] Albertus D. Handoko,[4] Sonal Kumar,[1] Wutthikrai Busayaporn,[5] Dechmongkhon Kaewsuwan,[5] Changyun Jiang,[1] Mingdeng Wei,[6] Guihua Yu,[2] Zhi Wei Seh [1]**

[a] Institute of Materials Research and Engineering (IMRE), Agency for Science, Technology and Research (A*STAR), 2 Fusionopolis Way, Innovis #08-03, Singapore 138634, Republic of Singapore.

[b] Materials Science and Engineering Program and Walker Department of Mechanical Engineering, The University of Texas at Austin, Austin, Texas, 78712, USA.

[c] Institute of High Performance Computing (IHPC), Agency for Science, Technology and Research (A*STAR), 1 Fusionopolis Way, #16-16 Connexis, Singapore 138632, Republic of Singapore.

[d] Institute of Sustainability for Chemicals, Energy and Environment (ISCE^2), Agency for Science, Technology and Research (A*STAR), 1 Pesek Road, Singapore 627833, Republic of Singapore.

[e] Synchrotron Light Research Institute, 111 Moo 6 University Avenue, Muang, Nakhon Ratchasima 30000, Thailand.

[f] Fujian Provincial Key Laboratory of Electrochemical Energy Storage Materials, Fuzhou University, Fuzhou, Fujian 350002, China.

*Corresponding author email: ghyu@austin.utexas.edu; sehzw@imre.a-star.edu.sg.

Progress and potential

Magnesium-ion batteries (MIBs) show great potential as an alternative to lithium-ion batteries for energy storage. However, the sluggish kinetics, originated from the strong electrostatic interactions between the high charge density of Mg^{2+} and host materials, has plagued the further development of MIBs. Owing to the low charge density of S and Se, transition metal chalcogenides (TMCs) are regarded as promising cathodes for Mg^{2+} that can weaken these detrimental interactions. Unfortunately, the shuttle effects of TMCs are known to degrade electrochemical performance. To facilitate TMC cathode design, we fabricate a heterostructure comprised of cobalt sulfide (Co_3S_4/CoS_2) hollow nanospheres, in which built-in electric fields generated in heterointerfaces boost the electronic conductivity, binding energies, and therefore the efficiency of Mg^{2+} migration. We found Co_3S_4 to have an adsorption effect on magnesium polysulfides, inhibiting the dissolution of these intermediates from CoS_2, which will significantly boost the performance of MIBs. As MIBs in pouch cells have been poorly studied, we examined the use of our MIB system in pouch cells. Our pouch cells produce an energy density of 203 Wh kg^{-1} after 100 cycles at 40 mA g^{-1}, strongly hinting practical application. The results of this study can pave the way for optimization of cathodes in MIBs.

Summary

Transition metal chalcogenides (TMCs) with *3d*-orbitals have been intensively studied for use as cathodes in magnesium-ion batteries. However, their poor electronic conductivities, and sluggish electrochemical kinetics severely restrict their electrochemical performance to prevent wide applicability for these materials. Here we propose a heterointerface structure of cobalt sulfide (Co_3S_4/CoS_2) hollow nanospheres to enable built-in electric fields generated in heterointerfaces, as also verified in density functional theory (DFT), finite element simulations (FES), and ab initio molecular dynamics (AIMD) results. Compared to other TMCs, our cathode exhibited a substantial capacity of 597 mAh g^{-1} after 120 cycles at 50 mA g^{-1}. When evaluated in a pouch cell, the electrode can sustain 100 deep cycles at 40 mA g^{-1}, with an energy density of 203 Wh kg^{-1} that displays potential for practical applications. Finally, rational heterostructure engineering of transition metal-based sulfides provides new insights into developing cathodes for high-performance sustainable Mg batteries.

Keywords: Heterojunction structure, cobalt sulfides, cathodes, magnesium-ion batteries

Introduction

Despite the massive global usage of lithium-ion batteries (LIBs), the drawbacks associated with LIBs such as safety and limitations in capacities have spurred extensive research in identifying and constructing suitable replacements.[1-7] To this end, many candidates to replace LIBs have been proposed including sodium, calcium, magnesium, as well as aluminum-ion batteries.[8-14] Among these, magnesium-ion batteries (MIBs) have been considered to be the most promising next-generation storage devices, owing to their low cost, high theoretical capacities, and low reduction potential (Mg/Mg^{2+}, -2.37 V *vs.* standard hydrogen electrode (SHE)).[15-17] Unfortunately, sluggish electrochemical kinetics resulting from strong electrostatic interactions between the lattices of host materials and multivalent ions (Mg^{2+}) continue to hinder the development of MIBs for practical applications.[18-21]

A number of solutions have been proposed to overcome these limitations, including the possible use of transition metal chalcogenide (TMC) cathodes, as the weak interaction between Mg^{2+} and low charge-density anions (e.g., S, Se, and Te) facilitates ion insertion.[22-24] Additionally, studies have revealed that transition metal cations and chalcogen anions can both undergo redox chemistry reactions in some TMCs to enhance the charge storage capability.[25-31] Conversely, the dissolution and diffusion of soluble polysulfide intermediates in TMCs reduce the capacity and cycling stability of MIBs. To date, little has been done to understand and inhibit the shuttle effect of magnesium polysulfides in TMC cathodes for MIBs. Overall, it remains a great challenge to construct TMC cathodes for prospective MIBs that offer high capacities, high energy densities, and long cycling stabilities.

Co-based sulfides (Co_9S_8, CoS, Co_3S_4, and CoS_2), especially Co_3S_4 and CoS_2, have been considered promising materials for battery electrodes, owing to their electrical conductivity and thermal stability.[32-35] The unique spinel structure of Co_3S_4 contains many intrinsic nanopores for hosting metal ions, with the Co atoms occupying both tetrahedral and octahedral sites to allow reversible insertion/deinsertion of metal ions.[36,37] At the same time, the presence of $(S_2)^{2-}$ in CoS_2, originating from the near band levels between the Co 3d and S 3p orbitals, enhances charge capacity owing to the anionic redox chemistry ($S^{2-}/(S_2)^{2-}$) involved.[38] We postulate that it would be promising to combine Co_3S_4 and CoS_2 in the form of hybrid heterostructures to achieve synergistic effects. However, previous studies on Co-based sulfides have only explored single-component Co_3S_4 or CoS_2 as MIB cathodes. Moreover, to the best of our knowledge, Co-based sulfides have been rarely studied in pure magnesium electrolytes without lithium salts.[26] Though the use of lithium salt additives helps to improve the sluggish reaction kinetics, it complicates the study of Mg insertion/conversion processes in TMC cathodes, leading to poor mechanistic understanding.

Here for the first time, we propose the rational construction of heterostructure interfaces in Co_3S_4/CoS_2 hollow nanospheres to be evaluated as cathodes in MIBs. Electron transport and Mg^{2+} mobility can be enhanced by the internal electric field, which are produced at two different energy band structures and Fermi levels in heterostructure interfaces. As such, the electrode (comprised of Co_3S_4/CoS_2 hollow nanospheres) exhibits excellent electrochemical performance in serving as cathodes in MIBs, even without lithium-based electrolyte additives. We found a high capacity of 597 mAh g^{-1} to be maintained after 120 cycles at 50 mA g^{-1}, which is a satisfactory cycling performance of TMCs in magnesium storage performance recorded under this current density. At a

larger current density of 100 mA g^{-1}, the electrode can also maintain a capacity of 483 mAh g^{-1} after 200 cycles, showing a respectable cycling stability. When tested at the pouch cell level, the full cell delivered a capacity of 152 mAh g^{-1} after 100 cycles at 40 mA g^{-1}, with a high energy density of 203 Wh $kg^{-1}_{(based\ on\ the\ mass\ of\ cathode)}$, that enhanced the possibility of practical applicability. Using ex-situ technologies of X-ray absorption spectroscopy, X-ray diffraction, and transmission electron microscopy revealed a reversible hybrid insertion/conversion mechanism of Co_3S_4/CoS_2 in the charge/discharge process, explaining the stability of its electrochemical processes. The mechanism of the charge/discharge process was also confirmed by calculation results of density functional theory (DFT), finite element simulation (FES), and ab initio molecular dynamics (AIMD). We believe that our strategy for fabricating heterostructure interfaces in Co_3S_4/CoS_2 hollow nanospheres can offer new insights to designing promising cathodes in MIBs.

Results and discussion

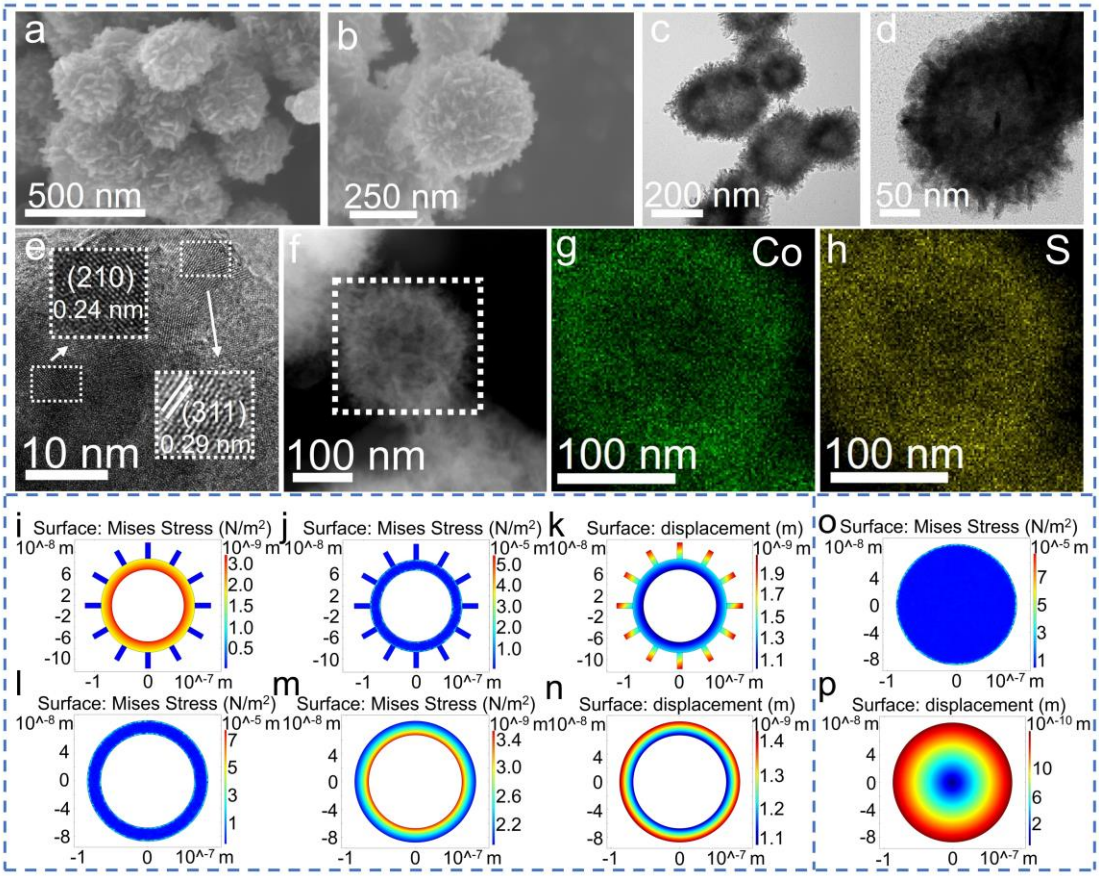

Figure 1. Characterization of morphology and simulation. (a, b) SEM images of Co_3S_4/CoS_2 hierarchical hollow spheres. (c, d, and e) TEM images and high-resolution TEM images of Co_3S_4/CoS_2 hierarchical hollow spheres, (f, g, and h) STEM image and corresponding elemental mapping images of Co and S, respectively. FE Simulations: (i-k) stress distributions (i) under external fixed boundary conditions, (j) under all fixed boundary conditions, (k) displacement under all free boundary conditions of hierarchical hollow nanospheres, (l-n) stress distributions (l) under external fixed boundary conditions, (m) under all fixed boundary conditions, (n) displacement under all free boundary conditions of hollow nanospheres, (o, p) stress and displacement distributions of solid spheres under all fixed and free boundary conditions.

We studied Co_3S_4/CoS_2 and Co_3S_4/CoS_2-8 that were prepared with different cobalt/sulfur precursor ratios (Co/S: 1/4 for Co_3S_4/CoS_2 and 1/8 for Co_3S_4/CoS_2-8). For comparison, Co_3S_4 was synthesized from Co_3S_4/CoS_2 treated at 400 °C for 2 h. The heterostructure Co_3S_4/CoS_2 hollow nanospheres

were prepared via a one-step solvothermal process (Figure S1) using Ostwald ripening. To ensure this mechanism of formation, samples with different reaction times (0.5, 4, and 8 h) were prepared. The scanning electron microscopy (SEM) images (Figure S2a-c) reveal the presence of irregular nanoparticles at a reaction time of 0.5 h (denoted as Co_3S_4/CoS_2-0.5 h). The nanoparticles were gradually formed and trace amounts of nanosheets were observed when the reaction time increased to 4 h (Figure S2d-f). Many hierarchical spheres composed of nanosheets were obtained when the reaction time reached 8 h (Figure S2g-i). The corresponding XRD patterns of these three samples (Co_3S_4/CoS_2-0.5 h, Co_3S_4/CoS_2-4 h, Co_3S_4/CoS_2-8 h) (Figure S3) suggest increased crystallinity in Co_3S_4/CoS_2 samples as the reaction proceeds. Based on these results, we postulate a gradual formation process of heterostructure Co_3S_4/CoS_2 hollow nanospheres. We verified the successful preparation of Co_3S_4/CoS_2 with XRD patterns and XPS characterization of the samples (Figure S4; Table S1; see supporting information).

The detailed morphology and structure of the Co_3S_4/CoS_2 hierarchical hollow nanospheres (Figure 1a-d) were elucidated with scanning electron microscopy (SEM) and transmission electron microscopy (TEM). The SEM image (Figure 1a) reveals that the hierarchical hollow nanospheres in Co_3S_4/CoS_2 are composed of interlaced nanosheets, suggesting a highly porous structure (Figure 1b). Meanwhile, the samples of Co_3S_4 and Co_3S_4/CoS_2-8 all maintain morphologies similar to that of Co_3S_4/CoS_2 (Figure S(5, 6)). The corresponding TEM images confirm the presence of hollow structures in the two samples (Co_3S_4 and Co_3S_4/CoS_2-8), indicating that the calcination process and the increasing amounts of sulfur in the preparation process have no effects on their formation (Figure S7).

The presence of a hollow interior in Co_3S_4/CoS_2 is confirmed (Figure 1c) with high resolution TEM, as the features of the nanosheet in the outer region of Co_3S_4/CoS_2 (Figure 1d). The interplanar lattice fringes of 0.29 nm and 0.24 nm observed in TEM images (Figure 1e inset) are separately attributed to (311) and (210) planes of Co_3S_4 and CoS_2 respectively, agreeing with results from XRD and XPS analyses. To further support the existence of Co_3S_4 and CoS_2 in Co_3S_4/CoS_2 composites, TEM images and corresponding selected area electron diffraction (SAED) patterns were collected from five different marginal places of Co_3S_4/CoS_2 hollow nanospheres (Figure (S8, S9)). The planes of (440), (422), and (311) are ascribed to the characteristics of Co_3S_4. And the plane of (210) is related to CoS_2, which is consistent with the observations made from HRTEM images. We further verified the hollowness of the nanospheres through the use of STEM and related line EDS images (Figure 1f inset), with the distribution of Co and S shown in the correlated EDS images of nanospheres (Figure 1g, 1h).

FE simulations were performed with regards to the morphologies of hierarchical hollow nanospheres, hollow spheres, and solid spheres of cobalt sulfides (Figures 1i-p). The modulated results show that with an external fixed boundary, the stress is distributed evenly around the hierarchical hollow spheres with an average value of $1.82 \times 10^{\wedge -9}$ N/m^2 (Figure 1i). The modulated stress within the interior of the hollow structure is higher than that of the outer region, in which the strain induced in the electrochemical process can be effectively retarded (Figure 1i). On the other hand, the hollow spheres exhibit a larger average stress of $2.50 \times 10^{\wedge -9}$ N/m^2 under the same condition (Figure 1l). For the all-fixed boundary conditions, the stress is distributed evenly around the entire hierarchical hollow sphere, with a maximum stress of $6.05 \times 10^{\wedge -5}$ N/m^2 (Figure

1j). Hollow and solid spheres demonstrate higher stress values of $8.59 \times 10^{\wedge -5}$ and $1.04 \times 10^{\wedge -4}$ N/m^2 respectively under the same condition (Figure 1m and 1o). The corresponding total displacement in hierarchical hollow nanospheres is smaller than that of simulated hollow and solid spheres (Figure 1k, 1n, and 1p). The FE mode results support the ability of well-designed hierarchical hollow nanospheres to effectively relieve the stress and displacement in the magnesiation process.

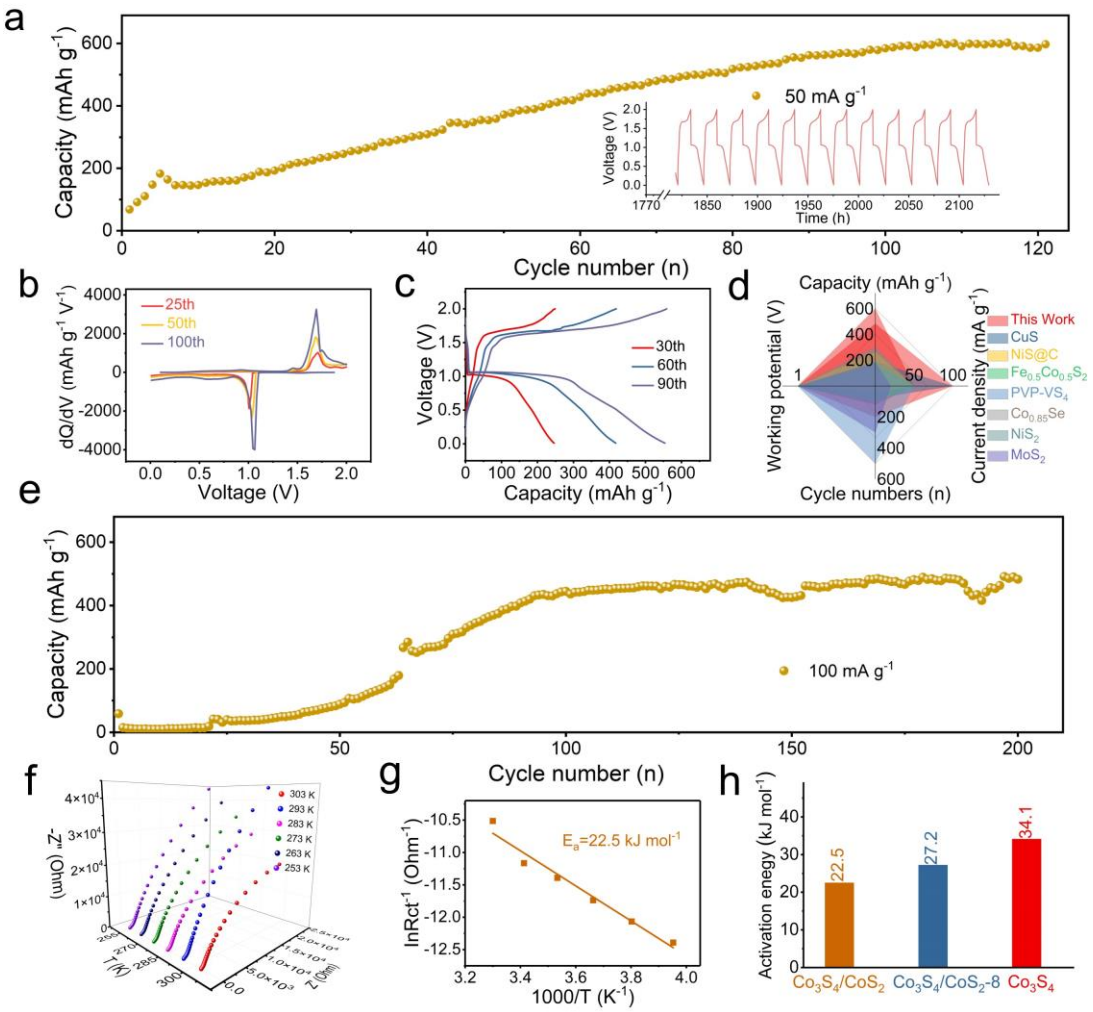

Figure 2. Electrochemical performances of cathodes. a) Cycling performance of Co_3S_4/CoS_2 at 50 mA g^{-1}, inset is the related Voltage-Time curves. b) The corresponding dQ/dV profiles of Co_3S_4/CoS_2 after different cycles. c) The corresponding charge-discharge curves after 30th, 60th, and 90th cycles. d) Electrochemical performance comparison of transition metal chalcogenides cathodes in MIBs. e) Cycling performance of Co_3S_4/CoS_2 at 100 mA g^{-1}. f) EIS of Co_3S_4/CoS_2 at varied

temperatures after 5 cycles. g) The related activation energy of Co_3S_4/CoS_2 after 5 cycles. h) The comparison of activation energy for Co_3S_4/CoS_2, Co_3S_4/CoS_2-8, and Co_3S_4.

To understand the structure of the Co_3S_4/CoS_2 heterojunction cathodes (Figure 2), we evaluated the electrochemical performance of the cobalt sulfide electrodes. At a current density of 50 mA g^{-1}, the Co_3S_4/CoS_2 electrode indicated a stable capacity of 597 mAh g^{-1} after 120 cycles, with a charge-discharge time of 2100 h (Figure 2a). By contrast, the Co_3S_4/CoS_2-8 and Co_3S_4/CoS_2-20 electrodes indicated lower capacities of 457 mAh g^{-1} after 40 cycles and 108 mAh g^{-1} after 80 cycles, respectively, while the Co_3S_4 electrode indicated the lowest capacity of 15 mAh g^{-1} after 200 cycles at 50 mA g^{-1} (Figure S10, S11, and S12). The cycling performances and corresponding Coulombic efficiencies indicate the advantage in Co_3S_4/CoS_2, in which the detrimental shuttle effects are also suppressed (Figure S13-16). The dQ/dV curves of Co_3S_4/CoS_2 show increased intensity after different cycles, a trend which suggests a stepwise activation process (Figure 2b). Moreover, the corresponding charge-discharge curves of Co_3S_4/CoS_2 after the 30^{th}, 60^{th}, and 90^{th} cycles show similar profiles when overlapped, pointing to a stable electrochemical process (Figure 2c). Notably, the Co_3S_4/CoS_2 electrode (Figure 2d) shows the highest capacity of 597 mAh g^{-1} at 50 mA g^{-1} compared to other TMC-based cathodes (Table S2).[22,25,39-43] Cycling stability is further demonstrated by the sustenance of 200 cycles with a capacity of 483 mAh g^{-1} at a current density of 100 mA g^{-1} (Figure 2e). The cycling performances of the Co_3S_4/CoS_2 hollow nanospheres were tested at 50 mA g^{-1}, using carbon paper and Al as collectors. The cathodes performed poorly electrochemically, highlighting the advantages of the Cu collector (Figure S17).[26,31,44-46]

To validate the electrochemical performance of Co_3S_4/CoS_2, electrochemical impedance spectra (EIS) at different temperatures (303 K, 293 K, 283 K, 273 K, 263 K, and 253 K) were obtained after

5 cycles (Figure 2f). The EIS of Co_3S_4/CoS_2 show the lowest activation energy of 22.5 kJ mol^{-1} (Figure 2g) [47] using the following equation:

$$i_o = A_o e^{\frac{-E_a}{RT}} \quad (1)$$

Where E_a is the activation energy, i_o is the exchange current density, T is the temperature, and R is the molar gas constant, and A_o is a constant character. In contrast, the EIS of Co_3S_4/CoS_2-8 and Co_3S_4 (Figure S18a, b) indicate the corresponding activation energies to be 27.2 kJ mol^{-1} and 34.1 kJ mol^{-1} (Figure 2h), based on the correlation plots between $InR_{ct}{}^{-1}$ and $1/T$ (Figure S19). We thus postulate that the lowest energy for Mg^{2+} migration and electron transfer resistance come from the heterostructure interfaces of Co_3S_4/CoS_2. CV curves at increased scan rates were plotted to investigate the capacity contribution from capacitance and diffusion-controlled processes (Figure S20). The correlation between redox peak current and scan rates is explained from the following equation:

$$i = av^b \quad (2)$$

In which i, a, and v represent peak current, constant, and scan rates, respectively. The values of b are calculated to be 0.59 and 0.90 from the reduction and oxidation peaks, respectively, indicating that the reduction and oxidation process are separately dominated by diffusion-controlled and capacitance effects. The specific contributions from diffusion-controlled and capacitance are estimated based on the following equation:

$$i = k_1 v + k_2 v^{1/2} \quad (3)$$

in which i, v, k_1, and k_2 are current, scan rates, constants, and constants, respectively. The capacity is mainly affected by diffusion-controlled process when the scan rate is below 1 mV s^{-1} (Figure S20).

Density functional theory (DFT) calculations have been used to elucidate the electrochemical performance of Co_3S_4/CoS_2. The density of states (DOS) for these three electrodes (Figure 3a-c) show

that CoS_2 is semi-metallic, i.e., the electron spin-up channel is metallic (no band gap) while the spin-down channel has a band gap, as shown in previous studies.[48] CoS_2 thus behaves as a conductor, and Co_3S_4 as a semiconductor. The resulting Co_3S_4/CoS_2 interface is also semi-metallic, i.e., the spin-up channel remains metallic, and the spin-down channel exhibits a reduced band gap as compared to CoS_2, showing the improved conductive nature of the interface. Meanwhile, the Mg insertion energy for Co_3S_4 is 0.16 eV (Figure S21), while that for CoS_2 is 1.17 eV (Figure S22). This means that the inserting Mg into the structure of CoS_2 is more exothermic (favorable) than doing the same for Co_3S_4. The calculated theoretical capacities for CoS_2 and Co_3S_4 are 653 mAh g^{-1} and 288 mAh g^{-1}, respectively. Thus, the Co_3S_4/CoS_2 heterostructure can combine the advantages of both Co_3S_4 and CoS_2 in substantially enhancing magnesium storage performance.

We obtained time-of-flight secondary ion mass spectrometry (TOF-SIMs) of Mg^+, Co^+, and S^+ distributions after full discharged/charged states to investigate the dynamic evolution process of Co_3S_4/CoS_2. The distribution of Mg^+ is stable between the internal and outer region at 0.01 V, while the intensity curves at open circuit voltage (OCV) and fully charged state (2.0 V) exhibit notable variations with sputtering time (Figure 3d-f). This is consistent with the expectations for Mg^{2+} insertion/de-insertion behaviors. The reconstructed 3D sputtered volume of the secondary ion fragments of Mg^+, Co^+, and S^+ at different potential states agree closely with observations for specific ions distributions (Figure 3g). We used a series of ex-situ studies to elucidate the storage mechanism of the discharge-charge process. Scanning transmission electron microscopy (STEM) (Figure 3h) confirms the maintenance of the hollow spherical structure during the discharge/charge process. This result indicates that the strain induced in the insertion/de-insertion of Mg^{2+} can be alleviated by the hollow structure, corroborating the results from the FE simulation. The corresponding EDS-mapping images of these electrodes reveal the even

distribution of the elemental Co, S, and Mg.

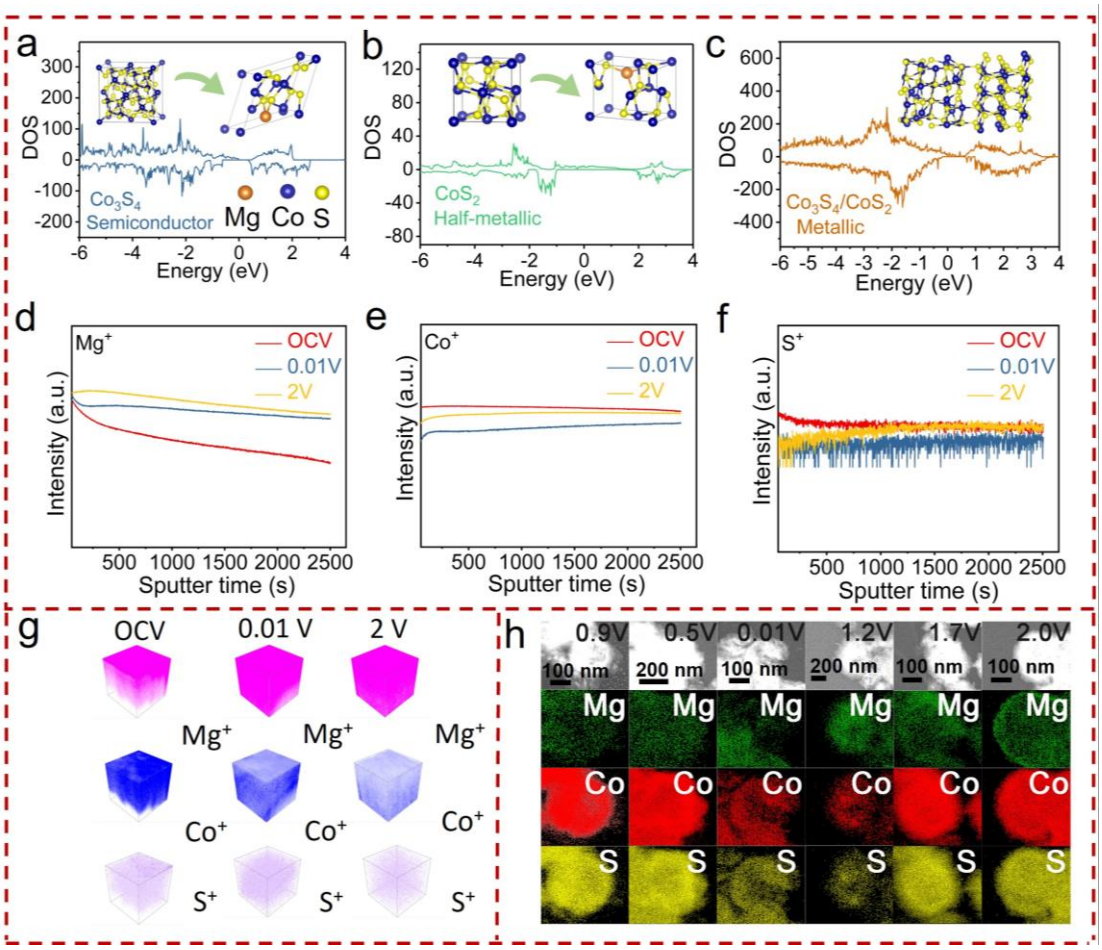

Figure 3. **Theoretical calculations and qualitative analyses of electrochemical process.** Band structures of (a) Co_3S_4, (b) CoS_2, and (c) Co_3S_4/CoS_2, respectively. TOF-SIMS normalized time profiling of several typical secondary ion fragments of (d) Mg^+, (e) Co^+, and (f) S^+, at different potential states. (g) 3D reconstruction of the sputtered volume of several secondary ion fragments of Mg^+, Co^+, and S^+ at different potential states. (h) EDS-mapping images of Co_3S_4/CoS_2 hollow spheres at different potentials in the discharge/charge process.

We investigated the mechanism of the discharge/charge process at the Co_3S_4/CoS_2 cathode using ex-situ TEM images, XAS spectra, and XRD patterns (Figure 4). When discharged to 0.9 V, the lattice fringes from the marginal areas of the Co_3S_4/CoS_2 hierarchical hollow spheres measured 0.17 nm and 0.28 nm, which have been separately assigned to (110) and (311) planes of CoS and Co_3S_4, respectively. (Figure

4a). During the discharging process to 0.5 V, we obtained the characteristic lattice fringe of (400) and (220) for Co_3S_4 (Figure 4b). At the end of the discharge cut-off voltage of 0.01 V, the lattice fringes measured 0.29 nm and 0.23 nm, which are ascribed to the presence of CoS and Co_3S_4 respectively (Figure 4c). During the reverse charge process, the typical lattice fringes of 0.17 nm and 0.19 nm were detected at 1.2 V, which are associated with the (440) and (102) planes for Co_3S_4 and CoS, respectively (Figure 4d). Charging to 1.7 V reveals the interplanar lattice for CoS_2, indicating the CoS_2 being gradually reformed. At the end-of-charge cut-off voltage (2.0 V), the characteristic (211) plane of CoS_2 is observed, indicating a hybrid conversion/insertion mechanism for Co_3S_4/CoS_2. X-ray absorption spectroscopy (XAS) of Co *K*-edge (Figure 4g) shows no obvious shift in the rising edge for discharge vs. charge samples, leading us to believe there is no significant change in the oxidation state of Co. Thus, we postulate that the hybrid conversion/insertion mechanism largely consists of the following two reactions:

$$Co_3S_4 + xMg^{2+} + 2xe^- \rightarrow Mg_xCo_3S_4\ ; \quad (4)$$

$$CoS_2 + Mg^{2+} + 2e^- \rightarrow CoS + MgS; \quad (5)$$

To further support the above proposed mechanism, we obtained ex-situ XRD patterns during the electrochemical process after 5 cycles (Figure 4h and Figure S23). In the discharge process, the peaks for CoS_2 weaken, accompanied by the emergence of peaks for CoS. When discharged to 0.01V, there are no peaks for CoS_2, but peaks for Co_3S_4 and CoS are present. During the corresponding charge process, there are no diffractions observed for CoS_2 until 2.0 V, while the peaks of Co_3S_4 are observed. This is attributed to the probable presence of reformed CoS_2. XPS spectra collected from different charge states are presented in Figure S24 to support the above observations. Notably, the evolved peaks of S^{2-} appeared at discharge state of 0.01 V, with the disappearance of $(S_2)^{2-}$. When charged to 2.0 V, the characteristic peaks of $(S_2)^{2-}$ and S^{2-} can be noticed. In contrast, there are no significant differences between the full

discharge (0.01 V) and charge states (2.0 V) in XPS spectra of Co 2p. Therefore, the XPS spectra results support our postulation that a hybrid storage mechanism is responsible during the discharge/charge process.

The oxidation states of Cu after discharge/charge states were also investigated with XPS spectra (Figure S25). The peaks of Cu 2p spectra for cathodes in a fully charged state (2.0 V) and Cu metal are at lower binding energies than those for cathodes in a fully discharged state, which are consolidated by the cryo-STEM, HRTEM and corresponding EDS mapping images (Figure S26).

These results support the occurrence of the reversible reaction:

$$Cu_xS + 2e^- + Mg^{2+} \leftrightarrow xCu + MgS \quad (6)$$

Previous studies have shown that the Cu collector has a positive effect on electrochemical performance via the evolution of Cu_xS.[26,31]

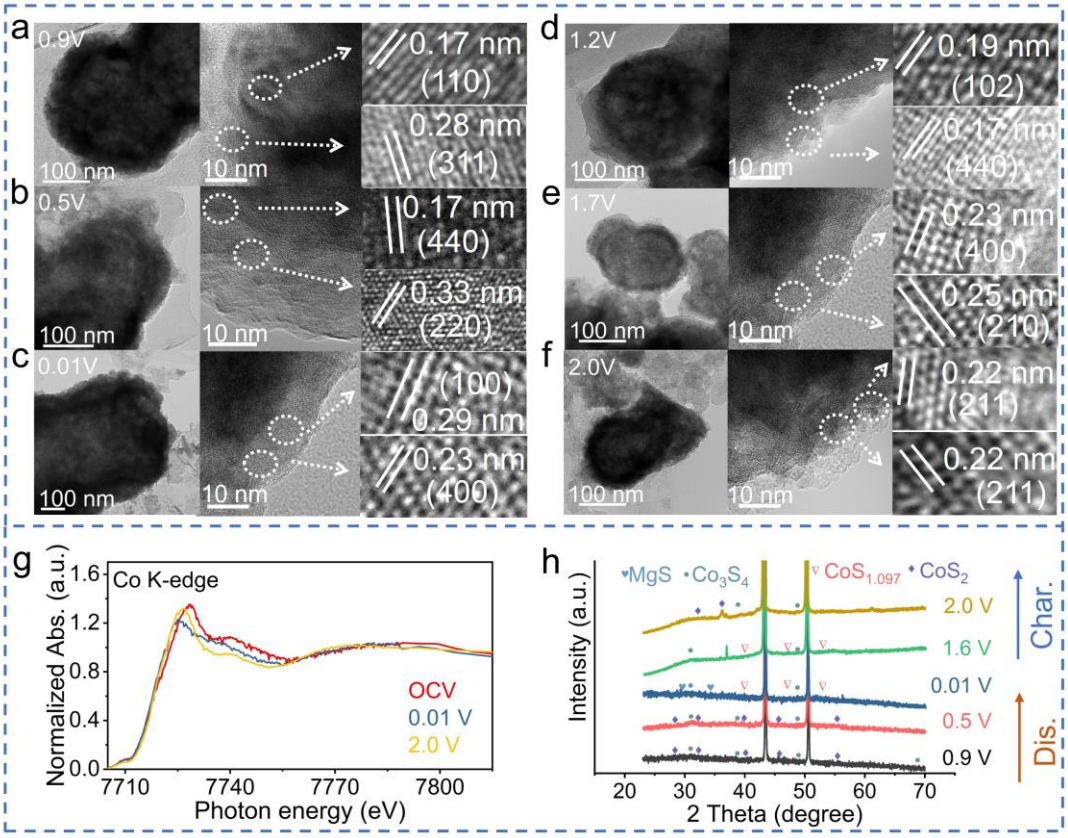

Figure 4. Structure evolution of Co_3S_4/CoS_2 during the electrochemical process. Ex-situ TEM images of Co_3S_4/CoS_2 at different potential of (a) 0.9 V, (b) 0.5 V, (c) 0.01 V, (d) 1.2 V, (e) 1.7 V, and (f) 2.0 V. Ex-situ (g) XAS spectrum, and (h) XRD patterns.

The structural stability of the Co_3S_4/CoS_2 hollow spheres are revealed by cryo-TEM, which is particularly suited for reducing beam damage in battery materials (Figure 5a-c). The integrity of the hollow structure can be maintained after 200 repeated insertion/extraction processes (Figure 5a, b), highlighting this advantage. The corresponding STEM-EDS mapping images demonstrate the even distribution of Co and S elements around the hollow spherical structure (Figure S27). The high-resolution TEM image reveals lattice fringes of 0.32 nm at different orientations, which are indexed to (111) plane of Co_3S_4 (Figure 5c). A pouch cell was assembled to evaluate the practical applicability of the cathode. To verify the flexibility of the pouch cell, the CV curves of pouch cells treated at different angles were found to share overlapping

profiles, indicating the electrochemical processes to be stable (Figure 5d, S28). When tested at a current density of 40 mA g^{-1}, the pouch cell indicated a capacity of 152 mAh g^{-1} after 100 cycles (Figure 5e), with a gravimetric energy density of 203 Wh kg^{-1}. The corresponding charge/discharge curves after the 80^{th} cycle show wider plateaus than in the 40^{th} and 20^{th} cycles, which agree closely with the activation cycling performance (Figure 5f). The electrochemical properties of cathodes in the magnesium-ion batteries at the pouch cell level (Table S3) demonstrate a competitive electrochemical performance in terms of capacity and cycling stability for Co_3S_4/CoS_2. [25,49-58]

The calculated adsorption energies between Co_3S_4 and MgS_x (x=1, 2, 4, 6, and 8) (Figure 5g) support this capacity and cycling stability.[59-61] The adsorption energies of -5.07 eV, -4.72 eV, -3.74 eV, -4.55 eV, and -4.16 eV calculated f Co_3S_4 and MgS_x (x=1, 2, 4, 6, and 8) are all negative and verify the presence of an adsorption effect between Co_3S_4 and MgS_x (Figure 5h). This adsorption effect inhibits the detrimental shuttle effects of soluble magnesium sulfide intermediates formed by CoS_2 during the conversion process, accounting for the excellent cycling stability of the Co_3S_4/CoS_2 cathodes. Results of ab initio molecular dynamics simulations (AIMD) conducted to further elucidate the dynamic evolution processes support this stable cycling performance (Figure 5 i-n). The interface modes of Co_3S_4-Mg, CoS_2-Mg, Co_3S_4-MgS_6 were constructed to monitor the dynamic variation kinetics. The Co_3S_4-Mg interface was found to be stable, with negligible inter-diffusion after 100 ps. In contrast, S atoms in CoS_2 can diffuse into the structure of the bulk Mg, with Mg atoms also reversibly diffusing into CoS_2 after 100 ps. These results indicate that CoS_2 reacts with Mg to form MgS_x, while Co_3S_4 works by insertion, without new compounds being formed. Using MgS_6 interacting with Co_3S_4 as an example, the Co_3S_4-MgS_6 interface was found to be stable, with minor changes observed after 100 ps. Some Mg atoms diffuse to the interfacial regions, but cannot diffuse into the Co_3S_4 region, which validates the adsorption effect

of Co_3S_4-MgS_6 observed through DFT calculations.

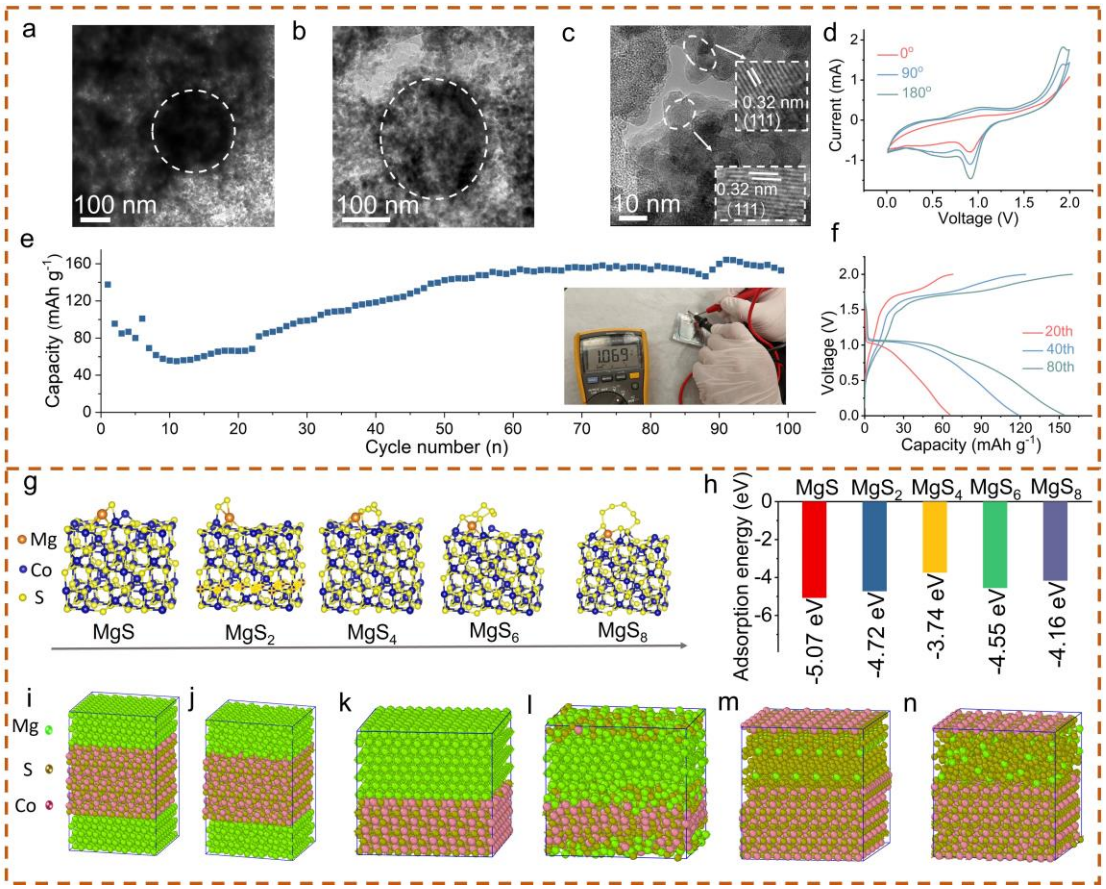

Figure 5. **Structure integrity characterization, pouch cell performances, DFT and AMID simulations.** (a-c) Cryo-TEM images of Co_3S_4/CoS_2 after 200 cycles, (d) CV curves at a sweep rate of 0.5 mV s^{-1} under different conditions, (e) cycling performance of RMBs pouch cell at 40 mA g^{-1}. Inset shows the pouch cell with an open circuit voltage of 1.01 V. (f) Charge-discharge profiles of pouch cell after 20^{th}, 40^{th}, and 80^{th} cycles. (g) Optimized atomic structures of MgS, MgS_2, MgS_4, MgS_6, and MgS_8 cluster adsorbed on facet of Co_3S_4. (h) The corresponding adsorption energies between Co_3S_4 and MgS_x (x=1, 2, 4, 6, and 8). Interface modes of (i, j) Co_3S_4-Mg, (k, l) CoS_2-Mg, and (m, n) Co_3S_4-MgS_6 before MD simulation and after MD simulation processes.

Conclusions

In this study, Co_3S_4/CoS_2 heterojunction hollow nanospheres were prepared via a one-step solvothermal process and used as cathodes in magnesium-ion batteries. We found the migration of Mg^{2+} to be enhanced by the heterojunction between Co_3S_4 and CoS_2, and the hollow nanostructure to retard large volume variation induced in the electrochemical process (supported by ex-situ TEM images and FE simulations). More importantly, we found an adsorption effect by Co_3S_4 on magnesium polysulfides, inhibiting their dissolution from CoS_2; this is confirmed by DFT and AIMD simulations. Consequently, we found the Co_3S_4/CoS_2 electrode to deliver a capacity of 597 mAh g^{-1} after 120 cycles at a current density of 50 mA g^{-1}. At a larger current density of 100 mA g^{-1}, a capacity of 483 mAh g^{-1} was maintained after 200 cycles. When evaluated in a pouch cell, a stable capacity of 152 mAh g^{-1} was retained after 100 cycles at 40 mA g^{-1}, showing promise for practical applicability. The hybrid electrochemical mechanism of conversion insertion has also been verified by ex-situ XRD patterns, TEM images, and XAS spectra during the discharge/charge process. The results of our study can point the way to the fabrication of high-performance cathodes in magnesium-ion batteries by retarding shuttle effects with metal sulfide heterojunctions.

Experimental procedures

Synthesis of Cobalt sulfides hollow nanospheres

Cobalt(II) acetylacetonate [$Co(AC)_2$, 0.257 g] was dispersed in 30 ml of isopropyl alcohol (IPA) and the solution stirred for about 5 mins. Thioacetamide (TAA; 0.3 g) was then added to the solution and stirred for 10 mins to obtain a homogeneous solution. The above mixture was transferred into a 50 ml stainless steel autoclave and the reaction maintained at 180 °C for 12 hours. The black pellet obtained after

centrifugation of the solution was washed several times with isopropyl alcohol (IPA) and then dried in a vacuum oven at 70 °C overnight to obtain Co_3S_4/CoS_2. Repeating the abovementioned steps, but with 0.6 g and 1.5 g of thioacetamide instead yielded Co_3S_4/CoS_2-8 and Co_3S_4/CoS_2-20, respectively. Co_3S_4 was obtained by calcinating Co_3S_4/CoS_2 at 400 °C for 2 h in an argon atmosphere. We used CoS_2 purchased from Sigma-Aldrich as a reference sample. The samples of Co_3S_4/CoS_2 for the refined XRD pattern were prepared by mixing the specific weight of Co_3S_4/CoS_2 with rutile TiO_2 in a weight ratio of 12.04 mg/100.6 mg. The Co_3S_4/CoS_2-8 used in refined XRD pattern was prepared following identical steps described above. Detailed information on calibrating XRD can be found in Supporting Information (SI).

Characterization of Materials

The crystalline structure was analyzed by X-ray diffraction (XRD, Bruker D8, with Cu-Kα radiation of 1.5418 Å). X-ray photoelectron spectroscopy (XPS, Thermo-scientific, with Al Kα radiation of 1486.6 eV) was used to analyze the elemental states. Information on morphologies and interior structures was obtained using scanning electron microscopy (SEM, Hitachi SU8200) and transmission electron microscopy (TEM, JEOL2100). Ex-situ TEM images and cryogenic electron microscopy (cryo-EM) images were obtained with a transmission electron microscope (TEM, TITAN AND TECHNAI). Ion distributions were determined with time-of-flight secondary ion mass spectrometry (IONTOF GmbH, Germany measurements).

Electrochemical Measurements

The electrochemical experiments were conducted using CR-2023 type coin cells and pouch cells, which were assembled in an argon filled glovebox. In preparing the cathode, Co_3S_4/CoS_2, carbon black, and

polyvinylidene difluoride (PVDF) were mixed in a weight ratio of 7:2:1 and hand milled for 30 mins. NMP was then added to obtain a homogenous slurry. Following this, the slurry was spread evenly on copper foil and dried in a vacuum oven overnight to obtain the cathode. A polypropylene Celgard membrane was applied as the separator. The electrolyte was composed of 0.5 M magnesium trifluoromethanesulfonate ($Mg(OTF)_2$) in 1,2-dimethoxyethane (DME) with the addition of 0.3 M tetrabutylammonium chloride (TBAC).[62,63] The electrolyte volume was 75 µl for each coin cell, and Mg foil was used as an anode. For the pouch cell, the electrolyte volume was increased to 400 ul. The charge-discharge curves were collected on a battery tester (Neware CT-3008). Cyclic voltammetry and electrochemical impedance spectroscopy were performed with an electrochemical workstation (Gamry Interface 1010E). The equation for calculating energy density can be found in the SI.

Density functional theory (DFT) calculations

See SI for detailed information on DFT calculations.

Finite Element Simulation (FIE) Method

See SI for detailed information on FIE calculations.

Ab Initio Molecular Dynamics (AIMD) Method

See SI for detailed information on AIMD calculations.

Acknowledgements

Z.W.S. acknowledges the Agency for Science, Technology and Research (MTC Programmatic Fund

M23L9b0052 and Central Research Fund Award). G.Y. acknowledges the support from the Welch Foundation Award F-1861 and Camille Dreyfus Teacher-Scholar Award. M.-F.N. and G.W. acknowledges the National Supercomputing Center (A*CRC) of Singapore using its high-performance computing facilities. M.W. acknowledges key project for technology innovation and industrialization of Fujian province (2023G002). The authors thank the technical assistance from Debbie Seng Hwee Leng in XPS as well as Zhenxiang Xing in time-of-flight secondary ion mass spectrometry (TOF-SIMs).

Author contributions

J.W., G. Y. and Z.W.S conceived the idea. J.W. performed the experiment and wrote the manuscript. Z. J. G. Y. and Z.W.S. revised the manuscript. T. G. conducted the TEM test. Z. J. and G. Y. analyzed Data. M. N. and G. W. performed DFT calculations and AMID simulations. G. Y. and X. Z. conducted XRD test. L. Z. performed the finite element method simulation. A. D. H. performed XRD calibration. S. K., W. B., and D. K. collected XAS spectra. C. J. and M. W. are involved in discussion and measurements.

Competing interests

The authors declare no competing interests.

References

1. Ju, Z., Checko, S., Xu, X., Calderon, J., Raigama, K.U., Takeuchi, K.J., Marschilok, A.C., Takeuchi, E.S., and Yu, G. (2023). Densified vertically lamellar electrode architectures for compact energy storage. Proc. Natl. Acad. Sci. U. S. A. *120*, e2308009120. 10.1073/pnas.2308009120.

2. Yao, Z., Lum, Y., Johnston, A., Mejia-Mendoza, L.M., Zhou, X., Wen, Y., Aspuru-Guzik, A., Sargent, E.H., and Seh, Z.W. (2022). Machine learning for a sustainable energy future. Nat. Rev. Mater. 1-14. 10.1038/s41578-022-00490-5.
3. Eng, A.Y.S., Soni, C.B., Lum, Y., Khoo, E., Yao, Z., Vineeth, S., Kumar, V., Lu, J., Johnson, C.S., and Wolverton, C. (2022). Theory-guided experimental design in battery materials research. Sci. Adv. *8*, eabm2422.
4. Liu, K., Liu, Y., Lin, D., Pei, A., and Cui, Y. (2018). Materials for lithium-ion battery safety. Sci. Adv. *4*, eaas9820.
5. Chen, H., Yang, Y., Boyle, D.T., Jeong, Y.K., Xu, R., de Vasconcelos, L.S., Huang, Z., Wang, H., Wang, H., Huang, W., et al. (2021). Free-standing ultrathin lithium metal–graphene oxide host foils with controllable thickness for lithium batteries. Nat. Energy *6*, 790-798. 10.1038/s41560-021-00833-6.
6. Cai, Z., Ou, Y., Zhang, B., Wang, J., Fu, L., Wan, M., Li, G., Wang, W., Wang, L., Jiang, J., et al. (2021). A Replacement Reaction Enabled Interdigitated Metal/Solid Electrolyte Architecture for Battery Cycling at 20 mA cm^{-2} and 20 mAh cm^{-2}. J. Am. Chem. Soc. *143*, 3143-3152. 10.1021/jacs.0c11753.
7. Guo, X., Ju, Z., Qian, X., Liu, Y., Xu, X., and Yu, G. (2023). A Stable Solid Polymer Electrolyte for Lithium Metal Battery with Electronically Conductive Fillers. Angew. Chem. Int. Ed. Engl. *62*, e202217538. 10.1002/anie.202217538.
8. Zhao-Karger, Z., Xiu, Y., Li, Z., Reupert, A., Smok, T., and Fichtner, M. (2022). Calcium-tin alloys as anodes for rechargeable non-aqueous calcium-ion batteries at room temperature. Nat. Commu. *13*, 1-9.
9. Wang, J., Huang, J., Huang, S., Notohara, H., Urita, K., Moriguchi, I., and Wei, M. (2020). Rational Design of Hierarchical SnS_2 Microspheres with S Vacancy for Enhanced Sodium Storage Performance. ACS Sustain. Chem. & Eng. *8*, 9519-9525. 10.1021/acssuschemeng.0c02535.
10. Yan, C., Lv, C., Wang, L., Cui, W., Zhang, L., Dinh, K.N., Tan, H., Wu, C., Wu, T., Ren, Y., et al. (2020). Architecting a Stable High-Energy Aqueous Al-Ion Battery. J. Am. Chem. Soc. *142*, 15295-15304. 10.1021/jacs.0c05054.
11. Yang, G., Li, Y., Zhang, C., Wang, J., Bai, Y., Lim, C.Y.J., Ng, M.F., Chang, Z., Kumar, S., Sofer, Z., et al. (2022). In Situ Formed Magnesiophilic Sites Guiding Uniform Deposition for Stable Magnesium Metal Anodes. Nano Lett. *22*, 9138-9146. 10.1021/acs.nanolett.2c03710.
12. Li, Y., Yang, G., Zhang, C., Lieu, W.Y., Lim, C.Y.J., Sun, S., Wang, J., Jiang, S., Xing, Z., Sofer, Z., et al. (2022). Grain-Boundary-Rich Triphasic Artificial Hybrid Interphase Toward Practical Magnesium Metal Anodes. Adv. Funct. Mater.. 10.1002/adfm.202210639.
13. Wang, J., Okabe, J., Urita, K., Moriguchi, I., and Wei, M. (2020). Cu_2S hollow spheres as an anode for high-rate sodium storage performance. J. Electroanal. Chem. *874*. 10.1016/j.jelechem.2020.114523.
14. Fan, W., Li, P., Shi, J., Chen, J., Tian, W., Wang, H., Wu, J., and Yu, G. (2023). Atomic Zincophilic Sites Regulating Microspace Electric Fields for Dendrite-Free Zinc Anode. Adv. Mater. e2307219. 10.1002/adma.202307219.
15. Dong, H., Tutusaus, O., Liang, Y., Zhang, Y., Lebens-Higgins, Z., Yang, W., Mohtadi, R., and Yao, Y. (2020). High-power Mg batteries enabled by heterogeneous enolization redox chemistry and weakly coordinating electrolytes. Nat. Energy *5*, 1043-1050. 10.1038/s41560-020-00734-

0.
16. Liang, Y., Dong, H., Aurbach, D., and Yao, Y. (2020). Current status and future directions of multivalent metal-ion batteries. Nat. Energy *5*, 646-656. 10.1038/s41560-020-0655-0.
17. Shin, C.H., Lee, H.Y., Gyan-Barimah, C., Yu, J.H., and Yu, J.S. (2023). Magnesium: properties and rich chemistry for new material synthesis and energy applications. Chem. Soc. Rev. *52*, 2145-2192. 10.1039/d2cs00810f.
18. Mao, M., Ji, X., Hou, S., Gao, T., Wang, F., Chen, L., Fan, X., Chen, J., Ma, J., and Wang, C. (2019). Tuning Anionic Chemistry To Improve Kinetics of Mg Intercalation. Chem. Mater. *31*, 3183-3191. 10.1021/acs.chemmater.8b05218.
19. Hou, S., Ji, X., Gaskell, K., Wang, P.-f., Wang, L., Xu, J., Sun, R., Borodin, O., and Wang, C. (2021). Solvation sheath reorganization enables divalent metal batteries with fast interfacial charge transfer kinetics. Science *374*, 172-178.
20. Huang, Y.X., Wu, F., and Chen, R.J. (2020). Thermodynamic analysis and kinetic optimization of high-energy batteries based on multi-electron reactions. Natl. Sci. Rev. *7*, 1367-1386. 10.1093/nsr/nwaa075.
21. Zhu, Y., Huang, G., Yin, J., Lei, Y., Emwas, A.H., Yu, X., Mohammed, O.F., and Alshareef, H.N. (2020). Hydrated $Mg_xV_5O_{12}$ Cathode with Improved Mg^{2+} Storage Performance. Adv. Energy Mater. *10*. 10.1002/aenm.202002128.
22. Wang, J., Handoko, A.D., Bai, Y., Yang, G., Li, Y., Xing, Z., Ng, M.F., and Seh, Z.W. (2022). High-Performance NiS_2 Hollow Nanosphere Cathodes in Magnesium-Ion Batteries Enabled by Tunable Redox Chemistry. Nano Lett. *22*, 10184-10191. 10.1021/acs.nanolett.2c04293.
23. Wang, D., Du, X., Chen, G., Song, F., Du, J., Zhao, J., Ma, Y., Wang, J., Du, A., Cui, Z., et al. (2023). Cathode Electrolyte Interphase (CEI) Endows Mo_6S_8 with Fast Interfacial Magnesium-Ion Transfer Kinetics. Angew. Chem. Int. Ed. Engl. *62*, e202217709. 10.1002/anie.202217709.
24. Xu, X., Ye, C., Chao, D., Davey, K., and Qiao, S.Z. (2023). Initiating Jahn–Teller Effect in Vanadium Diselenide for High Performance Magnesium-Based Batteries Operated at −40 °C. Adv. Energy Mater. *13*. 10.1002/aenm.202204344.
25. Mao, M., Tong, Y., Zhang, Q., Hu, Y.S., Li, H., Huang, X., Chen, L., Gu, L., and Suo, L. (2020). Joint Cationic and Anionic Redox Chemistry for Advanced Mg Batteries. Nano Lett. *20*, 6852-6858. 10.1021/acs.nanolett.0c02908.
26. Shen, Y., Zhang, Q., Wang, Y., Gu, L., Zhao, X., and Shen, X. (2021). A Pyrite Iron Disulfide Cathode with a Copper Current Collector for High-Energy Reversible Magnesium-Ion Storage. Adv. Mater. *33*, e2103881. 10.1002/adma.202103881.
27. Yuan, Z., Lin, Q., Li, Y., Han, W., and Wang, L. (2023). Effects of Multiple Ion Reactions Based on a $CoSe_2$/MXene Cathode in Aluminum-Ion Batteries. Adv. Mater. *35*, e2211527. 10.1002/adma.202211527.
28. Zhang, Y., Yuan, Z., Zhao, L., Li, Y., Qin, X., Li, J., Han, W., and Wang, L. (2023). Review of Design Routines of MXene Materials for Magnesium-Ion Energy Storage Device. Small *19*, e2301815. 10.1002/smll.202301815.
29. Lin, Q., and Wang, L. (2023). Layered double hydroxides as electrode materials for flexible energy storage devices. J. Semicond. *44*. 10.1088/1674-4926/44/4/041601.
30. Wang, J., Yang, G., Ghosh, T., Bai, Y., Lim, C.Y.J., Zhang, L., Seng, D.H.L., Goh, W.P., Xing, Z., Liu, Z., and Seh, Z.W. (2024). Hierarchical FeS_2 cathode with suppressed shuttle effect for high performance magnesium-ion batteries. Nano Energy *119*. 10.1016/j.nanoen.2023.109082.

31. Xu, H., Li, Y., Zhu, D., Li, Z., Sun, F., Zhu, W., Chen, Y., Zhang, J., Ren, L., Zhang, S., et al. (2022). Synchrotron Radiation Spectroscopic Studies of Mg^{2+} Storage Mechanisms in High-Performance Rechargeable Magnesium Batteries with Co-Doped FeS_2 Cathodes. Adv. Energy Mater. *12*. 10.1002/aenm.202201608.
32. Aslam, M.K., Seymour, I.D., Katyal, N., Li, S., Yang, T., Bao, S.J., Henkelman, G., and Xu, M. (2020). Metal chalcogenide hollow polar bipyramid prisms as efficient sulfur hosts for Na-S batteries. Nat. Commun. *11*, 5242. 10.1038/s41467-020-19078-0.
33. Lu, X.F., Zhang, S.L., Shangguan, E., Zhang, P., Gao, S., and Lou, X.W.D. (2020). Nitrogen-Doped Cobalt Pyrite Yolk-Shell Hollow Spheres for Long-Life Rechargeable Zn-Air Batteries. Adv. Sci. (Weinh) *7*, 2001178. 10.1002/advs.202001178.
34. Li, H., Yang, H., Sun, Z., Shi, Y., Cheng, H.-M., and Li, F. (2019). A highly reversible Co3S4 microsphere cathode material for aluminum-ion batteries. Nano Energy *56*, 100-108. 10.1016/j.nanoen.2018.11.045.
35. Ma, D., Hu, B., Wu, W., Liu, X., Zai, J., Shu, C., Tadesse Tsega, T., Chen, L., Qian, X., and Liu, T.L. (2019). Highly active nanostructured CoS_2/CoS heterojunction electrocatalysts for aqueous polysulfide/iodide redox flow batteries. Nat. Commun. *10*, 3367.
36. Guo, C., Zhang, W., Liu, Y., He, J., Yang, S., Liu, M., Wang, Q., and Guo, Z. (2019). Constructing CoO/Co_3S_4 Heterostructures Embedded in N-doped Carbon Frameworks for High-Performance Sodium-Ion Batteries. Adv. Funct. Mater. *29*. 10.1002/adfm.201901925.
37. Pan, Q., Tong, Z., Su, Y., Qin, S., and Tang, Y. (2021). Energy Storage Mechanism, Challenge and Design Strategies of Metal Sulfides for Rechargeable Sodium/Potassium-Ion Batteries. Adv. Funct. Mater. *31*. 10.1002/adfm.202103912.
38. Zhuang, R., Huang, Z., Wang, S., Qiao, J., Wu, J.-C., and Yang, J. (2021). Binder-free cobalt sulfide@carbon nanofibers composite films as cathode for rechargeable aluminum-ion batteries. Chem. Eng. J. *409*. 10.1016/j.cej.2020.128235.
39. Chen, D., Du, F., Cao, S.-a., Li, T., and Xu, F. (2022). $Co_{0.85}Se$ hollow polyhedrons entangled by carbon nanotubes as a high-performance cathode for magnesium secondary batteries. Chem. Eng. J. *428*. 10.1016/j.cej.2021.129545.
40. Du, C., Zhu, Y., Wang, Z., Wang, L., Younas, W., Ma, X., and Cao, C. (2020). Cuprous Self-Doping Regulated Mesoporous CuS Nanotube Cathode Materials for Rechargeable Magnesium Batteries. ACS Appl. Mater. Interf. *12*, 35035-35042. 10.1021/acsami.0c09466.
41. Zhu, G., Xia, G., Pan, H., and Yu, X. (2022). Size-Controllable Nickel Sulfide Nanoparticles Embedded in Carbon Nanofibers as High-Rate Conversion Cathodes for Hybrid Mg-Based Battery. Adv. Sci. (Weinh) *9*, e2106107. 10.1002/advs.202106107.
42. Zhuo, S., Huang, G., Sougrat, R., Guo, J., Wei, N., Shi, L., Li, R., Liang, H., Shi, Y., Zhang, Q., et al. (2022). Hierarchical Nanocapsules of Cu-Doped MoS_2@H-Substituted Graphdiyne for Magnesium Storage. ACS Nano *16*, 3955-3964. 10.1021/acsnano.1c09405.
43. Ding, S., Dai, X., Li, Z., Wang, C., Meng, A., Wang, L., Li, G., Huang, J., and Li, S. (2022). PVP-induced synergistic engineering of interlayer, self-doping, active surface and vacancies in VS_4 for enhancing magnesium ions storage and durability. Energy Storage Mater. *47*, 211-222. 10.1016/j.ensm.2022.02.023.
44. Xu, H., Zhang, X., Xie, T., Li, Z., Sun, F., Zhang, N., Chen, H., Zhu, Y., Zou, X., Lu, C., et al. (2022). Li^+ assisted fast and stable Mg^{2+} reversible storage in cobalt sulfide cathodes for high performance magnesium/lithium hybrid-ion batteries. Energy Storage Mater. *46*, 583-593.

10.1016/j.ensm.2022.01.041.

45. Li, B., Li, Z., Chen, H., Zhang, X., Wu, S., Xu, H., Yao, Y., Li, Y., Li, X., Hu, Z., et al. (2022). Li^+ additive accelerated structural transformation of MoS_2 cathodes for performance-enhancing rechargeable Mg^{2+} batteries. Mater. Today Energy *27*. 10.1016/j.mtener.2022.101047.
46. Chen, H., Xu, H., Li, B., Li, Z., Zhang, K., Zou, J., Hu, Z., and Laine, R.M. (2022). Using amorphous CoS hollow nanocages as cathodes for high-performance magnesium-lithium dual-ion batteries. Appl. Surf. Sci. *598*. 10.1016/j.apsusc.2022.153768.
47. Wang, J., Huang, J., Huang, S., Komine, Y., Notohara, H., Urita, K., Moriguchi, I., and Wei, M. (2022). Regulating the effects of SnS shrinkage in all-solid-state lithium-ion batteries with excellent electrochemical performance. Chem. Eng. J. *429*. 10.1016/j.cej.2021.132424.
48. Shishidou, T., Freeman, A.J., and Asahi, R. (2001). Effect of GGA on the half-metallicity of the itinerant ferromagnet CoS_2. Phys. Review B *64*. 10.1103/PhysRevB.64.180401.
49. Mao, M., Gao, T., Hou, S., Wang, F., Chen, J., Wei, Z., Fan, X., Ji, X., Ma, J., and Wang, C. (2019). High-Energy-Density Rechargeable Mg Battery Enabled by a Displacement Reaction. Nano Lett. *19*, 6665-6672. 10.1021/acs.nanolett.9b02963.
50. Lu, D., Liu, H., Huang, T., Xu, Z., Ma, L., Yang, P., Qiang, P., Zhang, F., and Wu, D. (2018). Magnesium ion based organic secondary batteries. J. Mater. Chem. A *6*, 17297-17302. 10.1039/c8ta05230a.
51. Zhang, Y., Cao, J.M., Yuan, Z., Xu, H., Li, D., Li, Y., Han, W., and Wang, L. (2022). $TiVCT_x$ MXene/Chalcogenide Heterostructure-Based High-Performance Magnesium-Ion Battery as Flexible Integrated Units. Small *18*, e2202313. 10.1002/smll.202202313.
52. Shen, Y., Wang, Y., Miao, Y., Li, Q., Zhao, X., and Shen, X. (2023). Anion-Incorporated Mg-Ion Solvation Modulation Enables Fast Magnesium Storage Kinetics of Conversion-Type Cathode Materials. Adv. Mater. *35*, e2208289. 10.1002/adma.202208289.
53. Hou, X., Shi, H., Chang, T., Hou, K., Feng, L., Suo, G., Ye, X., Zhang, L., Yang, Y., and Wang, W. (2021). Hollow opening nanoflowers MoS_2-CuS-EG cathodes for high-performance hybrid Mg/Li-ion batteries. Chem. Eng. J. *409*. 10.1016/j.cej.2020.128271.
54. Shen, Y., Wang, Y., Miao, Y., Yang, M., Zhao, X., and Shen, X. (2020). High-Energy Interlayer-Expanded Copper Sulfide Cathode Material in Non-Corrosive Electrolyte for Rechargeable Magnesium Batteries. Adv. Mater. *32*, e1905524. 10.1002/adma.201905524.
55. Dey, S., Lee, J., Britto, S., Stratford, J.M., Keyzer, E.N., Dunstan, M.T., Cibin, G., Cassidy, S.J., Elgaml, M., and Grey, C.P. (2020). Exploring Cation-Anion Redox Processes in One-Dimensional Linear Chain Vanadium Tetrasulfide Rechargeable Magnesium Ion Cathodes. J. Am. Chem. Soc. *142*, 19588-19601. 10.1021/jacs.0c08222.
56. Zhang, Y., Li, Y., Wang, Y., Guo, R., Liu, W., Pei, H., Yin, G., Ye, D., Yu, S., and Xie, J. (2019). A flexible copper sulfide@ multi-walled carbon nanotubes cathode for advanced magnesium-lithium-ion batteries. J. Colloid Interf. Sci. *553*, 239-246. 10.1016/j.jcis.2019.06.027.
57. Pan, M., Zou, J., Laine, R., Khan, D., Guo, R., Zeng, X., and Ding, W. (2019). Using CoS cathode materials with 3D hierarchical porosity and an ionic liquid (IL) as an electrolyte additive for high capacity rechargeable magnesium batteries. J. Mater. Chem. A *7*, 18880-18888. 10.1039/c9ta05233j.
58. Shu, Q., Hou, X., Hou, K., Ye, X., Cao, Q., Li, D., and Suo, G. (2023). VS_4/MoS_2 cathodes with long cycle life and high rate performance for hybrid magnesium-lithium batteries. J. Alloys and Compd. *966*. 10.1016/j.jallcom.2023.171584.

59. Wang, L., Jankowski, P., Njel, C., Bauer, W., Li, Z., Meng, Z., Dasari, B., Vegge, T., Lastra, J.M.G., Zhao-Karger, Z., and Fichtner, M. (2022). Dual Role of Mo_6S_8 in Polysulfide Conversion and Shuttle for Mg-S Batteries. Adv. Sci. (Weinh) *9*, e2104605. 10.1002/advs.202104605.

60. Paul, A., Pandey, M., and Johari, P. (2023). Computational study of adsorption of magnesium polysulfides on VS4 magnesium sulfur batteries. Mater. Today: Proceed. *76*, 352-358. 10.1016/j.matpr.2022.11.399.

61. Yang, Y., Fu, W., Zhang, D., Ren, W., Zhang, S., Yan, Y., Zhang, Y., Lee, S.J., Lee, J.S., Ma, Z.F., et al. (2022). Toward High-Performance Mg-S Batteries via a Copper Phosphide Modified Separator. ACS Nano. 10.1021/acsnano.2c09302.

62. Nguyen, D.-T., Eng, A.Y.S., Horia, R., Sofer, Z., Handoko, A.D., Ng, M.-F., and Seh, Z.W. (2022). Rechargeable magnesium batteries enabled by conventional electrolytes with multifunctional organic chloride additives. Energy Storage Mater. *45*, 1120-1132. 10.1016/j.ensm.2021.11.011.

63. Yang, G., Li, Y., Wang, J., Lum, Y., Lim, C.Y.J., Ng, M.-F., Zhang, C., Chang, Z., Zhang, Z., and Handoko, A.D. (2024). Realizing horizontal magnesium platelet deposition and suppressed surface passivation for high-performance magnesium metal batteries. Energy & Environ. Sci. *17*, 1141-1152.